# Morphological Instability of a Confined Polymer Film in a Thermal Gradient

**Erik Schäffer,**[†,§] **Stephan Harkema,**[†] **Monique Roerdink,**[†] **Ralf Blossey,**[‡] **and Ullrich Steiner*,**[†]

*Department of Polymer Chemistry and Materials Science Center, University of Groningen, Nijenborgh 4, NL-9747 AG Groningen, The Netherlands and Zentrum für Bioinformatik, Universität des Saarlandes, D-66123 Saarbrücken, Germany*

*Received July 10, 2002*

ABSTRACT: We report the experimental observation of a morphological instability of a confined polymer−air double layer sandwiched between two plates set to different temperatures. The homogeneous temperature gradient across the double layer causes the breakup of the polymer film into columns or stripes spanning the two plates. Experimentally, the characteristic wavelength of these patterns varies with the inverse of the initial heat flux through the bilayer. To gain insight into the nature of the instability, we have developed a phenomenological model that describes the heat flow in terms of diffusion through the bilayer. In an idealized microscopic model for the heat flow through the bilayer system, thermal modes in the polymer film with wavelengths ranging from the film thickness to the Debye limit contribute to the heat flux. The low end of this frequency spectrum causes a thermal radiation pressure at the polymer−air surface that destabilizes the film, while the high-frequency modes ascertain the heat conduction through the bilayer.

## 1. Introduction

Pattern formation caused by instabilities of liquid interfaces either in the form of hydrodynamic instabilities[1] or as instabilities in thin films often result in similar morphologies despite differing driving mechanisms. The recent interest in thin film instabilities was partially triggered by technological importance of thin films, but also because surface instabilities allow to detect forces that are difficult to measure directly. A widely studied example that demonstrates the effect of interfacial forces are thin polymer films dewetting from a solid[2−5] or liquid substrate.[6] Here, film instabilities either occur spontaneously, driven by van der Waals forces,[9] or are homogeneously[7−10] or heterogeneously nucleated.[11,12] The origin of heterogeneous nucleation in glassy polymer films is still a matter of considerable speculation. Apart from the force balance, which determines the characteristic morphology that is formed after the film has ruptured, the dewetting dynamics yields information on the hydrodynamic boundary conditions at the film interfaces. Both slip and no-slip boundary conditions have been reported.[13] In addition to film instabilities driven by intermolecular forces, film breakup caused by electrostatic forces[14−16] have also been observed.

As opposed to the rupture of films by heterogeneous nucleation (which is characterized by the appearance of stochastically distributed holes), a spontaneous film instability shows a surface undulation with a characteristic wavelength that leads to the film breakup. The well-defined wavelength of this capillary wave is a signature of the force balance at the film surface, where the destabilizing force acts against the surface tension that tends to minimize the surface area. The onset of such a film instability is well described by a linear stability analysis, by which the hydrodynamic response of the film surface to a perturbation of its interfacial position is determined.

Here, we describe a thin film instability caused by a temperature gradient applied across a film in a confined geometry. A thin polymer film, placed between two flat plates that leave an air gap shows a morphological instability with a well-defined length scale.

On the basis of this observation we have investigated the origins of this instability both experimentally and theoretically. In the Experimental Section, we describe a systematic study of the dependence of the characteristic instability wavelength on the system parameters. To elucidate the origins of the instability, we have developed a theoretical model based on the identification of the mechanism of breakup, which we argue is the diffusive heat transport in the polymer−air bilayer. We develop a phenomenological description of this instability, and formulate an idealized microscopic model of this transport process to quantify the morphological transition from the bilayer to complex patterns spanning between the plates. The theoretical model described here extends a preliminary account in ref 17.

## 2. Experimental Section

**2.1. Materials.** The polymer used was polystyrene (PS) with an averaged molecular weight of 108 kg/mol and a polydispersity of 1.03, purchased from Polymer Standards Service, Mainz, Germany, and used as obtained. PS films were spin-cast onto highly polished silicon wafers (Wacker Siltronic, Burghausen, Germany). As received, the silicon wafers were covered with a native (≈2 nm thick) oxide layer. The materials properties are listed in Table 1. Prior to film deposition, the wafers were cleaned in a jet of $CO_2$ ice crystals (snow-jet[18]). Some substrates were covered with a gold layer by first evaporating 1−2 nm of Cr, followed by ≈100 nm of Au. A second silicon wafer was rendered unpolar by depositing an alkane self-assembled monolayer from solution.[19] Au was

* Corresponding author. E-mail: u.steiner@chem.rug.nl.
† University of Groningen.
‡ Universität des Saarlandes.
§ Present address: Max Planck Institute of Molecular Cell Biology and Genetics, 01307 Dresden, Germany.

**Table 1. Material Properties**

|     | $\kappa_i$ [J/(ms K)] | $u_i$ (m/s) | $\rho_i$ (kg/m³) | $\nu_D$ (THz) |
|-----|-----------|---------|---------|---------|
| air | 0.034 | 430 | 0.69 | |
| PS | 0.16 | 1850[a] | 984 | 3 |
| Si | 124 | 8400 | 2330 | 28 |
| Au | 317 | 3240 | 19 300 | 11 |

[a] For temperatures above the glass transition temperature of PS, $u_p \approx 1200$ m/s for $\nu \to 0$. Since we expect polymers to be glassy at high enough frequencies (see section 4), a value for $u_p$ that is typical for glassy PS was used.
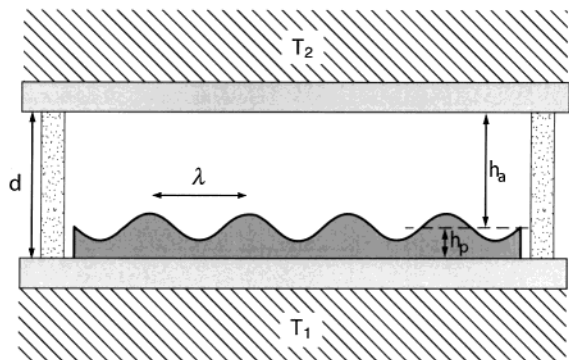


**Figure 1.** Schematic representation of the experimental setup. A liquid polymer film is destabilized by a heat flux across the film, which is the consequence of the applied temperature difference between the top and bottom plate. Silicon oxide spacers maintain a constant range of plate spacings $d$ in a wedge geometry (i.e., $d$ varies slightly from left to right).

evaporated onto the backside of all silicon wafers, to facilitate the short-circuiting of the two plates.

**2.2. Setup.** A schematic representation of the experimental setup is shown in Figure 1. The polymer-covered wafer was placed onto a temperature controlled hot plate set to 170 °C. Facing the polymer film (film thickness $h_p$), a second, unpolar wafer was mounted, leaving an air gap $h_a$. The distance $d = h_p + h_a$ between the two plates was kept constant by silicon oxide spacers that were sputtered onto the top wafer. Typically, $d$ varied by $\approx 1$ μm over a lateral distance of $\approx 1$ cm, allowing us to perform experiments with a range of $d$ values in a single run. As a heat sink, a water cooled copper block was placed onto the assembly. To ensure good thermal contact, thermally conducting paste was used between both the heat source and the cold sink and the two wafers. In addition, the two wafers were electrically short circuited to rule out film instabilities caused by electrostatic charges. Both temperatures $T_1$ and $T_2$ were kept constant within 1 °C.

Typical experimental parameters were values of $h_p$, $d$, and $\Delta T = T_1 - T_2$ ranging from 80 to 110 nm, from 100 to 600 nm, and from 10 to 55 °C, respectively. This resulted in a temperature gradient of $\sim 10^8$ °C/m. Samples were typically annealed overnight and then quenched to room temperature. After the top plate was removed, the morphology of the polymer was investigated by optical microscopy (in reflection mode) and tapping mode atomic force microscopy (AFM). Because of the reduced adhesion of the polymer on the self-assembled monolayer, all the polymer remained on the bottom wafer when disassembling the two plates, as confirmed by optical microscopy and AFM.

**2.3. Results.** Using the sample setup in Figure 1, two different film morphologies were observed as shown in Figure 2. The heat flow across the gap resulted either in polymer columns spanning the two plates (early stage, Figure 2a; late stage, Figure 2b) or in a stripe pattern (Figure 2c,d). We discuss Figure 2a,b first. For a given set of parameters ($h_p$, $d$, $\Delta T = T_1 - T_2$; see Figure 1), the column diameter ($1.9 \pm 0.2$
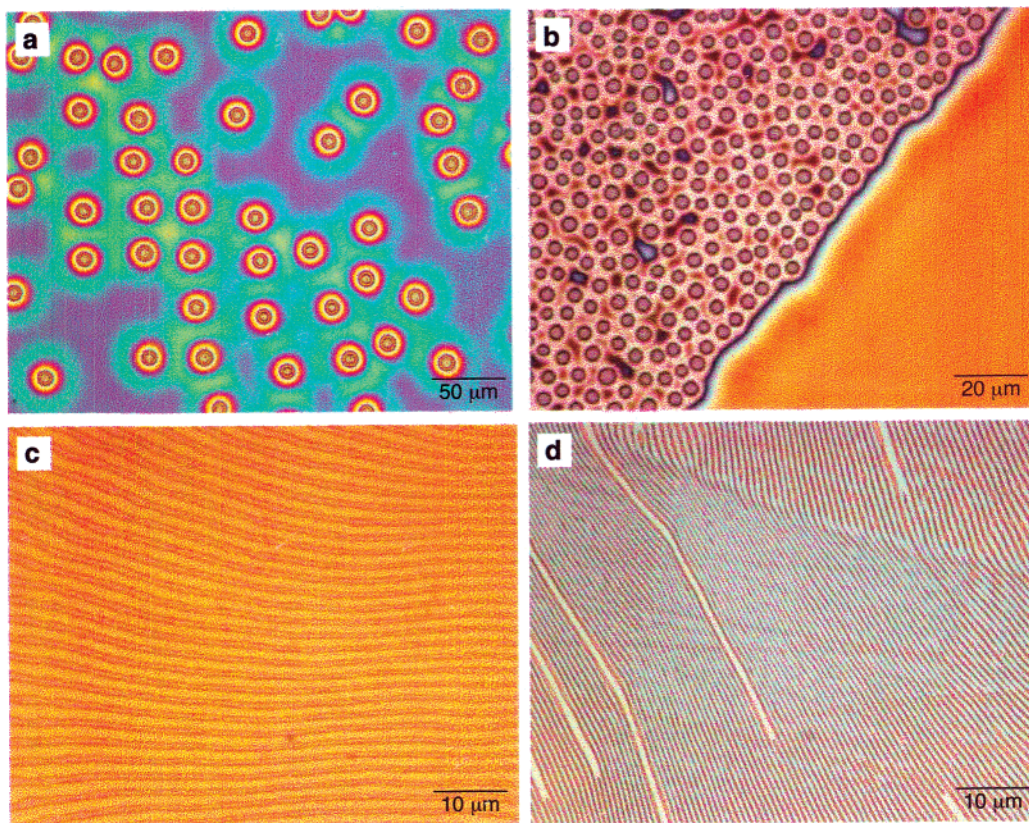


**Figure 2.** Optical micrographs of polystyrene films which were heated in the setup shown in Figure 1. Columnar and striped patterns were observed, often on the same sample. The formation of columnar patterns are shown in parts a (early stage) and b (late stage). The striped pattern in parts c and d typically showed a linear or spiral (not shown here) morphology. Experimental parameters: (a) $h = 309$ nm, $d = 755$ nm, $\Delta T = 28$ °C; (b) $h = 210$ nm, $d \approx 360$ nm, $\Delta T = 29$ °C; (c) $h = 130$ nm, $d \approx 250$ nm, $\Delta T = 19$ °C; (d) $h = 108$ nm, $d \approx 150$ nm, $\Delta T = 23$ °C. The colors stem from the constructive interference of the white microscope illumination and are an indication of the local film thickness.
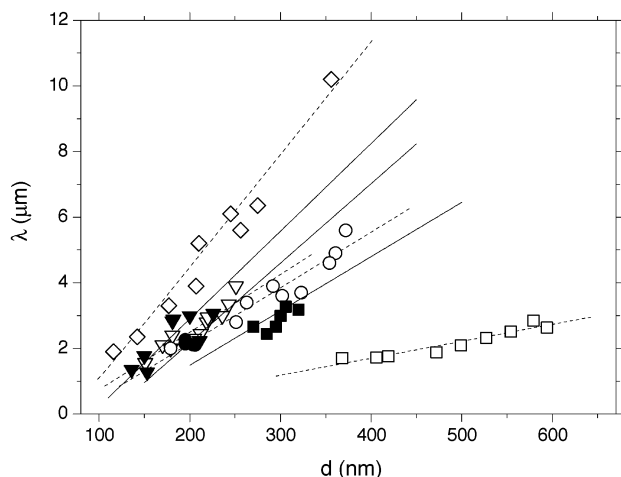
**Figure 3.** Plot of the experimentally determined instability wavelength $\lambda$ vs the plate spacing $d$. The open diamonds, triangles, and circles (data taken from ref 17) correspond to polystyrene films with $h = 96$ nm, $\Delta T = 11$ °C, $h = 80$ nm, $\Delta T = 43$ °C, and $h = 100$ nm, $\Delta T = 46$ °C, respectively. The solid triangles, squares, and circles stem from experiments (PS on Si) with $h = 130$ nm, $\Delta T = 28$ °C, $h = 130$ nm, $\Delta T = 60$ °C, and $h = 108$ nm, $\Delta T = 23$ °C, respectively. The open squares[17] represent a 92 nm thick polystyrene film which was spin-coated onto a gold (100 nm) covered silicon substrate ($\Delta T = 37$ °C).

$\mu$m) in Figure 2a was well-defined, while the columns themselves were stochastically distributed with an inter-column spacing $\lambda = 2.9 \pm 0.6$ $\mu$m (Figure 2b).

The morphology of the columns contains qualitative information about the breakup of the film. The well-defined column diameter in Figure 2a shows that the instability which led to the column formation occurred at a well-defined time. The stochastic column distribution indicates the absence of inter-column interactions. With time, the columns coalesced to form a more coarse grained columnar morphology that minimizes the polymer–air surface area. This process also led to a wider distribution of column sizes. As opposed to the structure formation driven by electric fields,[15] the columns in Figure 2a,b were connected by a thin polymer film. This enabled a lateral ripening process which is observed in Figure 2b.

The polymer morphologies in Figure 2 are a direct consequence of the applied temperature gradient. To ensure this, control experiments were performed in which similar samples were annealed in an oven ($\Delta T < 1$ °C). Oven-annealed films were stable for much longer times compared to the films in Figure 2. The film breakup that eventually occurred by heterogeneous nucleation leads to a very different film morphology.[4] The polymer morphology of a dewetting film between two confining plates will be subject of an upcoming publication.[20] Also, an experiment without a top plate ($d \rightarrow \infty$) did not show the film instability reported here.

A quantitative analysis of images similar to those in Figure 2 is shown in Figure 3. The characteristic spacing $\lambda$ can be obtained either by a Fourier analysis of the column and stripe patterns or (as done here) by directly measuring the distance between the columns and the stripes, in regions of homogeneous column or stripe distribution. Within the limits of the scatter of the data, $\lambda$ scales linearly with $d$. In addition, $\lambda$ is a decreasing function of the applied temperature difference $\Delta T$. An experiment was also performed with a polymer film that was deposited onto a gold surface (100 nm of Au on a silicon wafer–squares in Figure 3). Surprisingly, the choice of substrate has a strong effect on the wavelength of the instability. For otherwise similar experimental parameters, $\lambda$ is lowered by a factor of $\approx 4$, compared to films that were directly spin-coated onto silicon wafers. We note already here that this effect is by far greater than can be explained by the change in van der Waals forces alone.

The experimental results in Figures 2 and 3 show clearly that a temperature gradient in the two plate geometry of

Figure 1 is the cause of a film breakup that exhibits a well-defined mode. This instability mode depends on the applied temperature difference and on the spacing $d$ of the two plates, indicating that the heat flow across the polymer–air layer is the parameter that controls $\lambda$.

## 3. Morphological Instability of the Polymer Film

**3.1. Origin of the Morphology Change.** The morphology of the polymer film shown in Figure 2a,b is reminiscent of patterns that result from a spontaneous (spinodal) film instability during dewetting of thin films[4,5] or electrohydrodynamic structure formation.[15,16] The character of the instability we observe in the polymer films exposed to a heat current is, however, fundamentally different. The usual dewetting process occurs as a transition from an unstable (or metastable) to a stable state, and is therefore governed by the free energy of the system. The film–air double layer system of our study is subject to a current and hence a nonequilibrium system, in which an equivalent of the Gibbs' free-energy is unavailable.[21] Also, the transition is strongly determined by the confined geometry of the system as the morphological transition in the film structure is suppressed when the upper surface is removed.

While other sources of the instability were excluded by the careful design of our experiments and by control experiments with no applied temperature gradient, it is nevertheless instructive to compare our experimental results in the light of other possible sources of the instability, especially in the variety of possibilities the heat flow can have on the system.

While the top plate could contribute to a van der Waals disjoining pressure for very small values of $h_a$, there should be a negligible effect for $h_a > 100$ nm. The same is true for an elastic instability due to stresses stored in the film during the spin-coating process. Both pressure terms cannot account for the linear variation of $\lambda$ with the plate spacing $d$ for values of $h_a$ as large as 500 nm in Figure 3. While electrostatic effects were ruled out by short-circuiting the two plates, the variation of $\lambda$ vs $d$ is very different in the case of electrohydrodynamic instabilities, showing a strongly nonlinear variation of $\lambda$ vs $d$.

In macroscopic liquids, heat transport occurs predominantly by convection, giving rise to the well understood convective instabilities. In our very thin, highly viscous films, however, Rayleigh–Bénard or Marangoni–Bénard convection are suppressed. The onset of convection is determined by the critical values of the dimensionless Rayleigh ($R = (\rho g \beta \Delta T h^3)/(\eta D_T)$) and Marangoni ($M = ((-d\gamma/d)\Delta T h)/(\eta D_T)$) numbers ($\rho$, $\beta$, $\eta$, $\gamma$, $D_T$ are the density, thermal volume expansion coefficient, viscosity, surface tension, thermal diffusivity, respectively, and $g$ is the gravitational acceleration).[1] For our experimental parameters, we have $R \sim 1 \times 10^{-13}$ and $M \sim 1 \times 10^{-6}$. Compared to the critical values for convection ($R_c \gtrsim 670$, $M_c \gtrsim 80$), $R$ and $M$ of the thin polymer films were lower by 16 and 8 orders of magnitude, respectively. The low values of $R$ and $M$ are due to the high viscosity of the polymer melt, combined with the submicrometer film thickness.[1]

Since at the relatively low temperatures of the experiments ($T \leq 170$ °C) the radiative heat transfer is negligible, we are therefore led to conclude that the transfer of heat in our double layer system takes place
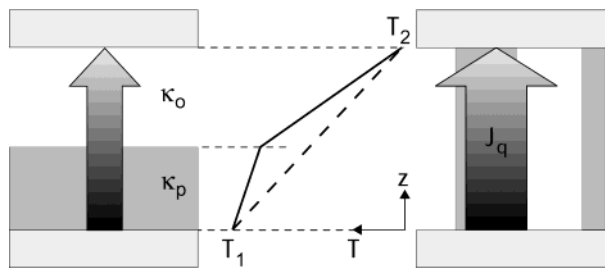
**Figure 4.** Schematic representation of the heat-flux for a polymer–air bilayer configuration (left) and a polymer morphology that spans the two plates (right). The temperature variation between $T_1$ and $T_2$ (middle) shows a kink for the bilayer situation (solid lines) and is continuous for a columnar or striped polymer morphology (right), thereby maximizing the heat flux.

essentially by heat diffusion. In the polymer film, heat diffusion occurs by the diffusion of local (segmental) molecular motion. Because of the high molecular weight of the polymer, the diffusion of entire polymer coils plays no role in the heat transport. In the air gap, thermal transport occurs by the translational diffusion of gas molecules.

**3.2. Phenomenological Description of the Polymer Film Morphology.** In this subsection, we formulate the basic phenomenological description of heat flow through the polymer–air bilayer. The heat current $J_q$ across the bilayer is given by Fourier's law

$$J_q = -\kappa \frac{\partial T}{\partial z} \tag{1}$$

with the thermal conductivity $\kappa$. For the double layer system in Figure 1, the temperature profile from $T_1$ to $T_2$ consists of a shallow gradient in the polymer ($\kappa_p$) and a steep gradient in the air layer ($\kappa_a$), as shown in Figure 4 (middle). For our system $\kappa_p/\kappa_a \approx 5$. $J_q$ within each layer is given by the linear equation $J_q = \kappa_i \Delta T_i / h_i$, with the heat conductivity $\kappa_i$, the temperature variation across the layer $i$ $\Delta T_i$, and the film thickness $h_i$. The thermal conductivities of the two plates are much larger than $\kappa_p$ and $\kappa_a$, so that the plates are isothermal. Since the overall heat flow is the same as the flux through the individual layers ($J_q = J_p = J_a$), we can solve for the interfacial temperature $T_i$

$$T_i = \frac{\kappa_p h_a}{\kappa_p h_a + \kappa_a h_p}(T_1 - T_2) \tag{2}$$

By eliminating $T_i$, we obtain

$$J_q = \frac{\kappa_a \kappa_p \Delta T}{\kappa_a h_p + \kappa_p h_a} \tag{3}$$

To investigate the morphology dependence of the heat flux, it is useful to first compare the initial and final morphologies (Figure 4) and their respective heat flow. Per unit area $\lambda^2$, mass conservation requires $\lambda^2 h_p = Ad$, where $A$ is the cross-sectional area through the columns (Figure 2a,b) with $A = 2\pi r^2/\sqrt{3}$ (assuming hexagonal packing with a column radius $r$), or through the stripes of width $w$ (Figure 2c,d) with $A = w\lambda$. The lateral morphology is, however not important since only the ratio of areas $\lambda^2/A = d/h_p$ enters in the balance of heat flow. For the final morphology, where the polymer is arranged in a way so that it spans the two plates, the heat flux is the sum of the heat conducted through the

polymer and the heat conducted through the air gap

$$J_q^f = \frac{h_p}{d}\frac{\kappa_p \Delta T}{d} + \left(1 - \frac{h_p}{d}\right)\frac{\kappa_a \Delta T}{d} \tag{4}$$

The ratio of the final to the initial (eq 3) flux is given by

$$\frac{J_q^f}{J_q} = 1 + \frac{(\kappa_p - \kappa_a)^2}{\kappa_a \kappa_p}\frac{h_p}{d}\left(1 - \frac{h_p}{d}\right) \tag{5}$$

By rearranging the polymer to a morphology where the polymer spans the two plates the heat flux between the two plates is increased. In a polystyrene–air double layer with $h_a = h_p$, for example, the heat flux is increased by a factor of $\approx 1.7$ when comparing the two film geometries in Figure 4, parts a and c.

While the maximization of the heat-flow (and thereby the maximization of the rate of entropy increase[22]) is not a sufficient condition to drive the system from the initial to the final configuration, it is a principle that is also observed in many other experimental systems[21] and is borne out by our experiments.

We now turn our attention to the two different morphologies observed in Figure 2. Columns (Figure 2a,b) and stripes (Figure 2c,d) were regularly observed, often on the same sample. Since both stripes and columnar morphologies are similar in terms of the effective heat conductivity between the two plates, an additional mechanism must be responsible for the morphology selection. The main difference between parts b and c of Figure 2 lies in the relative amount of PS/air interface (side walls), such that the surface energy of the walls provides an additional criterion to consider. We find per unit area $\lambda^2$ for the side wall areas $W$

$$W_{col} = \frac{4\pi}{\sqrt{3}} rd \tag{6a}$$

$$W_{line} = 2\lambda d \tag{6b}$$

for columns and lines, respectively. Since we have $\lambda^2 h_p = Ad$ and $A = 2\pi r^2/\sqrt{3}$

$$W_{col} = 2\lambda\sqrt{\frac{2\pi}{\sqrt{3}}h_p d} \tag{7}$$

The ratio

$$\frac{W_{col}}{W_{line}} = \sqrt{\frac{2\pi}{\sqrt{3}}\frac{h_p}{d}} \tag{8}$$

therefore provides a simple selection criterion for columns and lines as a function of the aspect ratio $d/h_p$. For values of the aspect ratio $d/h_p > 2\pi/\sqrt{3} \approx 3.6$ the columnar morphology has a lower side wall area per unit area, and lines are preferred for $d/h_p < 3.6$.

This principle is illustrated in Figure 5. In Figure 5a, the cross over from a column to a line morphology is shown. In Figure 5b, a histogram of column and line morphologies vs the $d/h_p$ ratio is shown. Keeping $h_p$ approximately constant (as in our experiments) columnar morphologies are more typically found for large
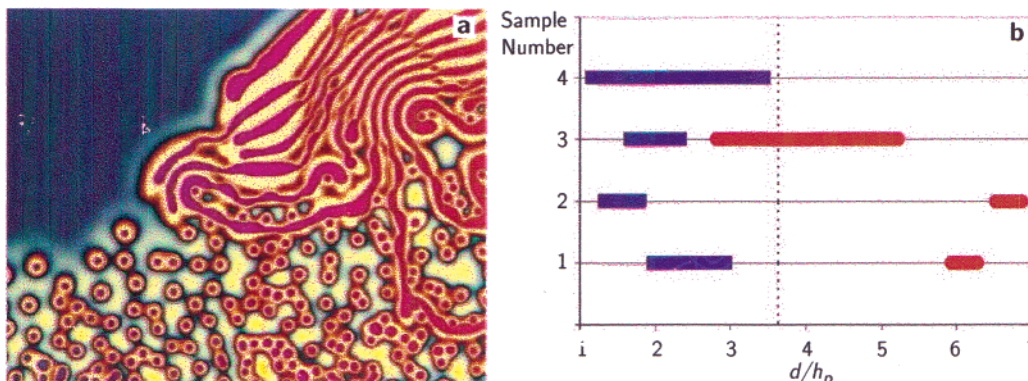
**Figure 5.** (a) Optical micrograph displaying the crossover from a column to a line morphology. (b) Diagram of line (blue) and column (red) morphologies vs the $d/h_p$ ratio for four different samples.

values of $d$, with lines more common for smaller plate spacings, in agreement with the simple surface energy argument.

**3.3. Instability of the Polymer–Air Interface in a Heat Flow.** Following a characterization of the observed patterns in terms of their heat flux and wall energetics, we must now elucidate the basic mechanism, which allows the system to evolve from the initial polymer–air bilayer structure to the configurations spanning the gap. This must clearly be caused by an instability of the polymer–air interface.

In the absence of convection, molecular vibrations in the liquid transport the heat. As postulated by Debye,[23] thermal excitations are high-frequency wave packets, comparable to phonons in crystalline solids. In this model, the flux of thermal energy $J_q$ causes a momentum flux in the direction of lower temperatures[24]

$$J_p = \frac{J_q}{u} \tag{9}$$

with the velocity of sound $u$. Acoustic radiation impinging on an interface between two media of different acoustic impedances causes a radiation pressure

$$p = -2R\frac{J_q}{u} \tag{10}$$

The magnitude and the sign of the reflectivity coefficient $R$ then determines whether the radiation pressure exerted by the heat flow is sufficient to destabilize the polymer–air interface.

At this point, is is necessary to discuss the nature of the momentum associated with waves in a medium, which often is a matter of confusion.[25] The Newtonian momentum of a volume of liquid stems from the net displacement of the liquid. The propagation of a longitudinal wave does, however, not result in a net displacement of the liquid. The symmetry operation where the liquid itself is stationary, but where a disturbance is translated through the medium can be described by the so-called "pseudo-momentum". The distinction between momentum and pseudo-momentum is necessary whenever a medium is involved. The pseudo-momentum is, however, subject to a similar conservation law as the "true" momentum. In fact, it is the conservation of pseudo-momentum that allows us to interpret the wave action in terms of the motion of phonons. The conservation of pseudo-momentum (and pseudo-energy) can be used to compute real forces.[25] For the boundary condi-
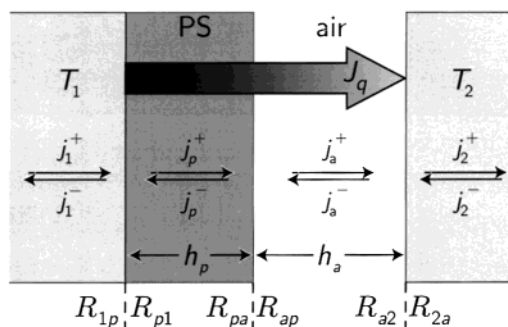


**Figure 6.** Partial heat flux components coupled in and out at the heat source (1) and sink (2) and in the polymer (p) and air (a) layer. The superscripts (+, −) indicate the direction of the heat flow. The boundary conditions for the heat diffusion in the four media is given by the interfacial reflectivities $R$.

tions of our experiment, the conservation of pseudo-momentum results in the Rayleigh radiation pressure in eq 10.

To achieve a description of the heat flow and the associated interfacial pressures in the bilayer system of Figure 1, the partial energy fluxes in each layer ($j_p^+$, $j_p^-$, $j_a^+$, $j_a^-$) and the fluxes that are coupled in and out of the heat source and sink have to be considered. This is shown schematically in Figure 6. The eight flux components are coupled by the reflection and transmission coefficients $R_{ik}$ and $\mathcal{T}_{ik} = 1 - R_{ik}$

$$j_i^- = \mathcal{T}_{i+1,i}\, j_{i+1}^- + R_{i,i+1}\, j_i^+ \tag{11a}$$

$$j_i^+ = \mathcal{T}_{i-1,i}\, j_{i-1}^+ + R_{i,i-1}\, j_i^- \tag{11b}$$

with the indices $i$, $k$, referring to the two layers (p, a) and the two plates (1, 2), and the numbering sequence in eq 11 1, p, a, 2. The net heat flux is given by

$$J_q = j_p^+ - j_p^- = j_a^+ - j_a^- \tag{12}$$

and the pressure acting at the polymer surface is

$$p = \frac{1}{u_a}\,(j_a^+ + j_a^-) - \frac{1}{u_p}\,(j_p^+ + j_p^-) \tag{13}$$

with $u_a$, $u_p$ the velocities of sound in air and the polymer film, respectively.

For our experimental conditions, we have $j_a^- \ll J_q$ (see section 4.1). We can then set $j_2^- \approx 0$ and $j_2^+ \approx J_q$. Using these boundary conditions, eqs 11 can be iteratively solved

$$j_1^+ = [(1 - R_{p1}R_{pa})(1 - R_{ap}R_{a2}) -$$
$$R_{p1}\mathscr{T}_{pa}\mathscr{T}_{ap}R_{a2}]\frac{1}{\mathscr{T}_{1p}\mathscr{T}_{pa}\mathscr{T}_{2a}}J_q \quad (14a)$$

$$j_1^- = [(\mathscr{T}_{1p}\mathscr{T}_{p1}R_{pa} + R_{1p}(1 - R_{p1}R_{pa}))(1 - R_{ap}R_{a2})$$
$$(14b)$$
$$+ (\mathscr{T}_{1p}\mathscr{T}_{p1} - R_{1p}R_{p1})\mathscr{T}_{pa}\mathscr{T}_{ap}R_{a2}]\frac{1}{\mathscr{T}_{1p}\mathscr{T}_{pa}\mathscr{T}_{2a}}J_q$$

$$j_p^+ = \frac{1 - R_{ap}R_{a2}}{\mathscr{T}_{pa}\mathscr{T}_{2a}}J_q \quad (14c)$$

$$j_p^- = \frac{\mathscr{T}_{pa}\mathscr{T}_{ap}R_{a2} + R_{pa}(1 - R_{ap}R_{a2})}{\mathscr{T}_{pa}\mathscr{T}_{2a}}J_q \quad (14d)$$

$$j_a^+ = \frac{1}{\mathscr{T}_{2a}}J_q \quad (14e)$$

$$j_a^- = \frac{R_{a2}}{\mathscr{T}_{2a}}J_q \quad (14f)$$

$$j_2^+ = J_q \quad (14g)$$

$$j_2^- = 0 \quad (14h)$$

Since $R_{ik}$ and $\mathscr{T}_{ik}$ are not dependent on $J_q$, the flux components $j_i^{\pm}$ are linear functions of $J_q$. Equation 13 therefore implies $p \sim J_q$. We thus assume that eq 10 is replaced by the phenomenological relation

$$p = -\frac{2\bar{Q}}{u_p}J_q \quad (15)$$

where $\bar{Q}$ is an acoustic quality factor of the polymer film. It is a function of the interfacial transmission and reflection coefficients. Solving eq 13 using eqs 14 and comparing to eq 15, we have

$$\bar{Q} =$$
$$\frac{((1 + R_{ap}) + R_{a2}(\mathscr{T}_{pa} - 2 R_{ap}))u_a - \mathscr{T}_{ap}(1 + R_{a2})u_p}{2 \mathscr{T}_{pa}T_{a2}u_a}$$
$$(16)$$

The values of $R_{ik}$ and $\mathscr{T}_{ik}$ specify the acoustic coupling of the four media[26] and determine the heat flow through the double layer. We will deal with this matter in detail in the following section.

On the basis of eq 15, the question whether the bilayer system is stable or not can be answered with a linear stability analysis.[2,3] To this end, the hydrodynamic response of the polymer film to a sinusoidal perturbation of its interfacial coordinate $h(x, t) = h_p + \zeta \exp(iqx + t/\tau)$ is calculated. The interfacial modulation causes a Poiseulle-type velocity profile in the polymer layer. The equation of motion for the interface is then given by the lubrication equation

$$\frac{\partial h(x, t)}{\partial t} = \frac{1}{3\eta}\frac{\partial}{\partial x}\left[h(x, t)^3\frac{\partial p}{\partial x}\right] \quad (17)$$

The linearization of eq 17 around the initial profile leads to the equation for the most unstable wavelength

$$\lambda = 2\pi\left(-\frac{1}{2\gamma}\frac{\partial p}{\partial h_p}\right)^{-1/2} \quad (18)$$
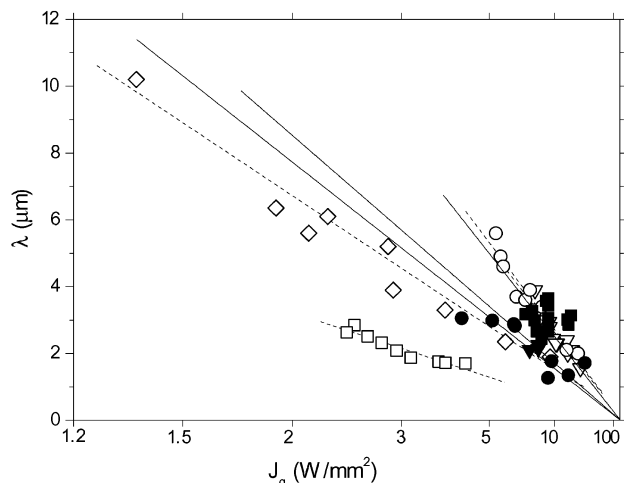


**Figure 7.** Data from Figure 3 plotted vs the heat flux $J_q$ on a reciprocal scale. The solid lines (dashed lines correspond to open symbols, solid lines to solid symbols) are the theoretical predictions from eq 19 with $\bar{Q} = 6.2$ for PS films on a silicon substrate and $\bar{Q} = 83$ for PS on gold (squares).

Using eqs 15 and 3, we obtain

$$\lambda = 2\pi\sqrt{\frac{\gamma u_p\Delta T}{\bar{Q}}\frac{\kappa_p\kappa_a}{(\kappa_p - \kappa_a)}\frac{1}{J_q}} \quad (19)$$

where $\gamma$ is the polymer−air surface tension (for PS, $\gamma = 30.0$ mN/m). Positive values of the quality factor $\bar{Q}$ lead to a destabilization of the polymer film. Our experimental results in Figure 7, the variation of the instability wavelength vs the inverse heat flux, lend strong support to our result of eq 19.

On the level of the phenomenological description, $\bar{Q}$ serves as a parameter that can be determined by a fit to the data. For the two systems studied here, we find $\bar{Q} \approx 6$ for the silicon/PS/air/silicon sandwich and $\bar{Q} = 83$ for the gold/PS/air/silicon system. Our results from the silicon/PS/air/silicon system confirm that $\bar{Q}$ does not depend on the geometrical parameters of the experiment or the applied temperature difference but exclusively on the material properties of the film and the plates. In other words, a single value of $\bar{Q}$ describes a large number of data sets.

It is instructive to compare the destabilizing pressure gradient exerted by the heat flux (i.e., the gradient of eq 15 with respect to $h_p$) to the pressure gradient stemming from the van der Waals forces ($p_{vdW} = A_{vdW}/(6\pi h_p^3)$). While polystyrene films on silicon are stabilized by the van der Waals pressure[9] we take the Hamaker constant $A_{vdW} = 1.8 \times 10^{-20}$ J for PS on glass. Assuming parameters characteristic for our experiments (see i.e., Figure 2), the comparison yields values of $\partial p/h_p$ of $O(10^{11})$ Pa/m and $O(10^7)$ Pa/m for the effect of the heat flux and the van der Waals term, respectively. Since the interfacial pressure gradient drives the interfacial instability (see eq 18), the destabilizing effect of van der Waals forces are negligible in our experiments. In other words, to account for the instability in Figure 2 by invoking a van der Waals model would imply unphysically large (by 4 orders of magnitude) Hamaker constants.

Using the $\bar{Q}$ values given above it is possible to rescale the data. In the framework of eq 19 it is convenient to define

$$J_0 = \frac{\kappa_a \kappa_p \Delta T}{(\kappa_p - \kappa_a) h_p} \qquad (20)$$

$$\lambda_0 = 2\pi \sqrt{\frac{\gamma u_p}{\bar{Q}} \frac{h_p}{J_0}} \qquad (21)$$

Equation 19 can then be written as

$$\frac{\lambda}{\lambda_0} = \left(\frac{J_q}{J_0}\right)^{-1} \qquad (22)$$

Plotted this way all our data collapses to a single master curve (see also the dashed line in Figure 8).

We can further improve this model by taking the temperature dependence of the surface tension into account. An undulating surface in our experimental setup is not isothermal. This implies that the surface tension is a function of the local film thickness of the polymer film. As a result, there is a surface free energy change associated with the instability. The surface stress is given by

$$p_\gamma = \frac{\partial \gamma}{\partial z}\bigg|_{z=h_p} = \frac{d\gamma}{dT} \frac{\partial T_i}{\partial h_p} \qquad (23)$$

Taking the derivative of eq 2 yields

$$\frac{\partial T_i}{\partial h_p} = -\frac{\kappa_a \kappa_p \Delta T d}{(\kappa_p h_a + \kappa_a h_p)^2} \qquad (24)$$

The derivative is negative and nonlinearly monotonically decreasing. In other words, for a symmetrical interface deformation (e.g., a sine wave), the temperature of an undulation maximum decreases more compared to the temperature increase in the minimum. Laterally averaged, this implies that the surface of an undulating film is effectively colder than a flat surface. Since the surface tension increases with decreasing temperature ($d\gamma/dT < 0$), an effectively colder surface implies an increased surface free energy. Consequently, $p_\gamma$ in eq 23 stabilizes the film.

The change in surface free energy can be incorporated into the theoretical framework described above. To this end, the overall pressure in eq 18 has to be taken as the sum of the thermomechanical pressure from eq 15 and the term stemming from the surface tension (eq 23). This introduces a correction factor into eq 19

$$\lambda = 2\pi \sqrt{\frac{\gamma u_p \Delta T}{\bar{Q}} \frac{\kappa_p \kappa_a}{(\kappa_p - \kappa_a)} \left(\frac{1}{1 + K J_q}\right) \frac{1}{J_q}} \qquad (25)$$

with

$$K = \frac{u_p d}{Q \Delta T \kappa_a \kappa_p} \left|\frac{d\gamma}{dT}\right| \qquad (26)$$

For the parameters of our experimental system, $K$ is only a small correction, since $d\gamma/dT \approx 0.07$ mN/m/K for PS. Qualitatively, the $p_\gamma$ term increases $\lambda$ by $\approx 10\%$.

This contribution introduces primarily an offset in $\lambda$ which can be incorporated into the $\lambda_0$ coefficient

$$\lambda_0 = 2\pi \sqrt{\frac{\gamma u_p}{\bar{Q}(1 - K)} \frac{h_p}{J_0}} \qquad (27)$$
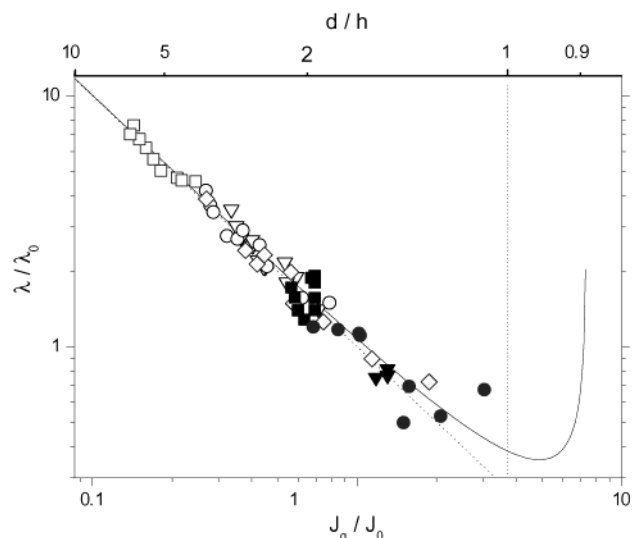


**Figure 8.** Characteristic wavelength $\lambda$ plotted vs the heat flux $J_q$ in reduced coordinates. The thin dashed line corresponds to to eq 22, taking $\bar{Q} = 6.2$ PS films on silicon and $\bar{Q} = 83$ for the PS on Au data set. The solid line is the prediction from eq 28 with $\bar{Q} = 6.7$ (Si) and $\bar{Q} = 84$ (Au). For small enough values of $d/h_p$ the interfacial pressure stemming from the surface tension ($p_\gamma$ in eq 23) dominates the heat flux driven pressure. For PS films, this occurs only for unphysical parameters: $d/h_p < 1$ (solid line).

with $K$ from eq 26. The master equation then also includes a $K$-dependent correction term

$$\frac{\lambda}{\lambda_0} = \frac{1}{\left(1 - \frac{K}{1-K} \frac{J_q}{J_0}\right)} \left(\frac{J_q}{J_0}\right)^{-1} \qquad (28)$$

Equation 28 is represented by the thick solid line in Figure 8. For high enough values of $J_q/J_0$, the deviation from the inverse scaling of $\lambda/\lambda_0$ with $J_q/J_0$ becomes visible. At very high values of $J_q/J_0$, eq 28 predicts a regime where the film is increasingly stabilized by the surface tension (i.e., $p_\gamma$). For our experimental parameters, however, this regime is predicted to occur only for the unphysical situation where $h_p > d$ (solid line in Figure 8).

An additional higher order correction is the effect of the temperature-dependent surface tension on the Laplace pressure. This could in principle lead to a lateral Marangoni flow of the polymeric liquid. The lateral variation in $p_\gamma$ introduces, however, only correction terms in the undulation amplitude of second and higher order. Since such higher order terms are negligible in the linear stability analysis, Marangoni flow does not play a role in the experimental situation described here.

We conclude from our phenomenological approach that our model describes the experimental results, however, with one fitting parameter, the acoustic quality factor $\bar{Q}$. We now turn to a microscopic derivation of $\bar{Q}$.

## 4. Heat Diffusion in a Polymer−Air Bilayer

A necessary requirement for the buildup of a phonon pressure—corresponding to a finite and positive $\bar{Q}$ factor—is a sufficiently large phonon mean free path in one of the two layers. This is the case for a polymer layer, for which mean free path lengths of 10 GHz phonons of several micrometers were reported in the literature.[27,28]

Since the phonon mean free path in the polymer film plays a central part in our argument, a frequency dependent model of the phonon propagation is needed. Qualitatively, this is a necessity, since phonon mean free path lengths are very short (comparable to an interatomic distance) in any material for thermal modes close to the Debye limit $\nu_D$. We must therefore differentiate between low and high-frequency phonons, and introduce a crossover frequency $\nu_c$ between these two regimes which is a priori unknown. A calculation of $\nu_c$ would require a detailed model of the phonon propagation in polymeric glasses, which to our knowledge does not exist. Measurements show, however, that phonons in glasses propagate acoustically up to several terahertz[29] and are specularly reflected off interfaces up to frequencies of several hundred gigahertz.[27,30] We therefore expect $\nu_c = O(\nu_D)$.

To treat the phonon propagation in the layer, simplifications are necessary, since the glassy character of the polymer at high acoustic frequencies complicates the discussion. For calculational simplicity, we assume a Debye mode spectrum in the polymer film. This clearly is an idealization since the density of states in glasses deviates in the lower terahertz region and exhibits a so-called "boson peak".[29]

A further consequence of the glassy response of a polymer melt at high frequencies is that transverse as well a longitudinal phonon modes have to be taken into account. In addition, angular dependencies of all modes need to be included. This leads to a similar theoretical framework (with a different value of $\bar{Q}$) as we develop here, but since it does not provide new insights, we neglect these effects to keep the calculation more transparent.

We now explore the details of the heat transport across the bilayer within this idealized Debye model of the phonon mode spectrum, which assumes the detailed balance of modes. We comment below on the repercussions of the latter assumption, again made for computational simplicity. In particular, we have to derive expressions for the six reflection coefficients that govern eqs 12 and 13. This is done in two steps. First, the conduction of heat though the air layer and the interfacial coupling from the air to the adjacent media is described, followed by a description of propagation of longitudinal waves (acoustic phonons) in the polymer film.

**4.1. The Gas—Liquid and Gas—Solid Interfaces.** Since the heat transport through the air layer by the diffusion of molecules differs significantly from the heat diffusion in the polymer film, it is reasonable to assume that the interfacial reflectivities are direction dependent. In particular, the polymer−air reflectivity $R_{pa}$ is different from the air−polymer reflectivity $R_{ap}$. The heat transfer from the gas to a solid or liquid is characterized by a so-called "accommodation coefficient", the fractional extent to which gas molecules that impinge onto a surface are energetically adjusted (or "accommodated") to the thermal energy of the wall.[31,32] This is opposed to the ballistic reflection of gas molecules, whereby only little thermal energy is exchanged between the gas molecule and the wall.

The fractional extent of accommodation is quantified by the accommodation coefficient

$$b = \frac{J_{inc} - J_{refl}}{J_{inc} - J_{acc}} \qquad (29)$$

where $J_{inc}$ is the incoming heat flux. Complete accommodation ($b = 1$) implies that the reflected heat flux $J_{refl}$ is identical to the energy flux of the molecules that have acquired the temperature of the wall, $J_{acc}$. If $b < 1$ some molecules are ballistically reflected without acquiring the temperature of the wall.

Since complete accommodation implies a perfect transmission of the thermal flux across the interface, we have in terms of the notation of eq 11: $R_{a2} = 1 - b_2$ and $R_{ap} = 1 - b_p$, where $b_2$ and $b_p$ are the accommodation coefficients at the heat sink ($T = T_2$) and the polymer surface, respectively.

$J_{acc}$ can be calculated from the kinetic theory of gases.[31] The translational energy carried by a stream of gas molecules that have the temperature $T_i$ of the solid or liquid medium at the interface is $2 RT_i$ per mol, where $R$ is the universal gas constant. The total energy of $S$ moles of such a stream is

$$J_{acc} = S(2RT_i + U_i) = S\left(\frac{1}{2}R + c_V\right)T_i \qquad (30)$$

where the internal energy $U_i$ is expressed in terms of the specific heat at constant volume $c_V = {}^3\!/_2 R + dU/dT$. The number of molecules in the stream is given by $S = {}^1\!/_4 \rho \bar{v} = p_0 / \sqrt{2\pi RT_i M}$, where $p_0$ is the atmospheric pressure and $M$ is the molecular mass of the gas molecules. Taking $c_V = {}^7\!/_2 R$ for a diatomic gas, we have

$$J_{acc} = p_0 \sqrt{\frac{8}{\pi}\frac{RT_i}{M}} \qquad (31)$$

For typical values of our experiment ($p_0 \approx 100$ Pa, $M \approx 29$ g/mol and $T_i \approx 400$ K), $J_{acc} \ll J_{inc} = J_q$, implying $j_2^- \approx 0$. We can use $R_{ap} \approx R_{a2} \approx 0$ (see below), which implies $J_{refl} \approx J_{acc}$, justifying our earlier assumption in section 3.3 that $j_a^- \ll j_a^+ \approx J_q$.

Experimentally, the heat transfer across an interface is sensitively dependent on the details of the interfacial parameters, with most data available at high vacuum conditions and clean metal surfaces. The closest parameters of such studies pertaining to our parameters are measurements for $N_2$ on water and platinum, which give values of the accommodation coefficient of 1 and 0.8, respectively.[31,33] The precise values of $R_{ap}$ and $R_{a2}$ turn out to be unimportant, since $\bar{Q}$ does not sensitively depend on them if they are close to zero.

**4.2. The Frequency Dependence of Thermal Diffusion.** As postulated above, the heat transport through the polymer film occurs by the diffusion of thermal segmental motion. Within a Debye model, this involves all frequencies up to the Debye limit, which corresponds to an acoustic wavelength comparable to an intermolecular spacing. We differentiate between two extreme cases.

**4.2.1. Acoustic Mismatch Model.** For relatively low acoustic frequencies ($\lesssim 100$ GHz), corresponding to wavelengths that are comparable to the film thickness, wave packets travel with a relatively long mean free path length between scattering events. In the case of polymers or even relatively low molecular weight oligomers, the mean free path is several micrometers at $\sim 10$ GHz. Such wave packets reflect acoustically off an interface with a reflectivity coefficient that is determined by the difference in acoustic impedances of the two media that form the interface[26]

$$R_{ik} = \left(\frac{Z_i - Z_k}{Z_i + Z_k}\right)^2 \tag{32}$$

$Z_i = \rho_i u_i$ is the acoustic impedance of medium $i$ with the density $\rho_i$. The acoustic reflection of phonons at the polymer−gas interface is nearly unity, mainly due to the large density differences between the two media. These phonons therefore exert a large destabilizing pressure on the interface. However, since they are nearly perfectly reflected, they do not contribute much to the total heat flow.

**4.2.2. Diffuse Mismatch Model.** While heat is conducted by the entire phonon spectrum, the predominant contribution stems from high-frequency phonons close to the Debye frequency $\nu_D = u_p(9n/4\pi)^{1/3}$, where $n$ is the number density. In this limit, the acoustic wavelength is comparable to an intermolecular length[27] (several Å) and the mean free path of the wave packets is very short ($\sim 1$ Å). In addition, on these length scales, the interface is not flat, but exhibits a spatial and temporal roughness. As a consequence, phonons are diffusively scattered at the interface. Rather than specular reflection given by eq 32, the transmission is determined by the differences in the density of states between the two media. Assuming detailed balance and longitudinal modes only, this results in[26]

$$\mathcal{T}_{ik} = \frac{u_i^2}{u_i^2 + u_k^2} \tag{33}$$

For the system in consideration, eqs 32 and 33 are opposing boundary conditions. Whereas low frequency phonons are almost completely reflected at the polymer−air surface ($R_{pa} \approx 1$), high frequency phonons that obey eq 33 are mostly transmitted ($\mathcal{T}_{ik} \approx 1$). These phonons are instrumental for heat conduction, but they exert only a small stabilizing interfacial pressure, partially compensating the effect of low-frequency phonons.

**4.3. Mode Dependent Heat Transport: Calculation of $\bar{Q}$.** While every phonon that is transmitted through the interface contributes equally to the total heat flux ($k_B T$ per phonon), the frequency dependent interfacial reflectivities lead to a frequency dependence of the net heat conduction per mode $j_q(\nu)$. In terms of the incoming flux, $j_q(\nu) = \hat{\mathcal{T}}(\nu)j_1^+$, defining the overall transmission $\hat{\mathcal{T}}$ through the polymer−air bilayer. Equation 14a yields

$$\hat{\mathcal{T}}(\nu) = \frac{\mathcal{T}_{1p}\mathcal{T}_{pa}\mathcal{T}_{a2}}{1 - R_{p1}R_{pa} - R_{ap}R_{a2} - R_{p1}R_{a2}(T_{pa} - R_{ap})} \tag{34}$$

$\hat{\mathcal{T}}(\nu)$ depends on all reflectivities, making the pressure dependent on the frequency and on the acoustic properties of all media, in particular of material of the heat source. In the low-frequency limit ($\nu \approx u_p/h_p$), where $R_{pa} \rightarrow 1$ (using $R_{ap} = R_{a2} = 0$), $\hat{\mathcal{T}}_l \approx \mathcal{T}_{1p}^l \mathcal{T}_{ap}^l / \mathcal{T}_{p1}^l$, while in the high-frequency limit ($\nu \approx \nu_D$) where $R_{pa} \rightarrow 0$, $\hat{\mathcal{T}}_h \approx \mathcal{T}_{1p}^h$. The indices l and h correspond to the low and high-frequency limits, respectively. Since $\mathcal{T}_{pa}^l \approx 0$ ($R_{pa} \approx 1$), low-frequency phonons contribute only little to the overall heat flux ($\hat{\mathcal{T}}_l \ll \hat{\mathcal{T}}_h$).

Making use of Debye's theory, the overall heat flux is

$$J_q(\nu) = C \int_0^{\nu_D} j_q \nu^2 \, d\nu \tag{35}$$

where $C$ is a constant (see below). While the mechanisms of heat flow through the bilayer in the low and high-frequency limit have been identified above, the detailed functional dependence of the crossover between these two regimes is not known.[26] As an approximation, we model the frequency dependence of the reflectivity coefficients as a step function, with a crossover frequency $\nu_c$

$$\hat{\mathcal{T}}(\nu) = \begin{cases} \hat{\mathcal{T}}_l \approx \dfrac{\mathcal{T}_{1p}^l \, \mathcal{T}_{ap}^l}{\mathcal{T}_{p1}^l} & \text{for } \nu \leq \nu_c \\[2ex] \hat{\mathcal{T}}_h \approx \mathcal{T}_{1p}^h & \text{for } \nu > \nu_c \end{cases} \tag{36}$$

where $\mathcal{T}_{ik}^l$ and $\mathcal{T}_{ik}^h$ are given by eqs 32 and 33, respectively. Using eq 36, the total heat flux is

$$J_q = C \int_0^{\nu_c} \hat{\mathcal{T}}_l j_1^+ \nu^2 \, d\nu + C \int_{\nu_c}^{\nu_D} \hat{\mathcal{T}}_h j_1^+ \nu^2 \, d\nu \tag{37}$$

Note that $J_q$ is given by eq 3, ensuring that macroscopically Fourier's law is obeyed.

Since the $\bar{Q}$ factor (eq 16) is a function of the frequency dependent reflectivities, it is also given in terms of a step function with the asymptotic values. Taking $R_{ap} = R_{a2} = 0$, we have

$$Q(\nu) = \begin{cases} Q_l \approx \dfrac{1}{\mathcal{T}_{pa}^l} & \text{for } \nu \leq \nu_c \\[2ex] Q_h \approx -\dfrac{1}{2}\left(\dfrac{u_p}{u_a} - 1\right) & \text{for } \nu > \nu_c \end{cases} \tag{38}$$

where $R_{pa} \rightarrow 0$. The relation for $Q_h$ was found by Gaeta et al.[24] for simple liquids. Typically, $Q_l = +O(1000)$ and $Q_h = -O(1)$. The different signs of $Q_l$ and $Q_h$ indicate that the radiation pressure of low-frequency phonons destabilizes the film, while the diffuse boundary conditions at high frequencies have a stabilizing effect.

Similar to the heat flux, the total interfacial pressure is obtained by integrating the mode dependent interfacial pressure over the phonon density of states

$$p = \int_0^{\nu_d} dp = -\frac{2C}{u_p}\int_0^{\nu_D} Q(\nu)j_q(\nu)\nu^2 d\nu \tag{39}$$

In terms of the frequency dependent $\hat{\mathcal{T}}$ and $Q$, this is written as

$$p = -\frac{2Cj_1^+}{u_p}\left[\int_0^{\nu_c} Q_l \hat{\mathcal{T}}_l \nu^2 d\nu + \int_{\nu_c}^{\nu_D} Q_h \hat{\mathcal{T}}_h \nu^2 d\nu\right] \tag{40}$$

By integrating eq 37, an expression for $Cj_1^+$ is obtained, which is inserted into eq 40. After integration of eq 40 and comparison to eq 15, an expression for the overall quality factor is obtained

$$\bar{Q} \approx \frac{f^3}{1 - f^3}\frac{\hat{\mathcal{T}}_l}{\hat{\mathcal{T}}_h}Q_l + Q_h \tag{41}$$

where we have introduced the ratio $f = \nu_c/\nu_D$ and made use of the fact that the heat flux is mediated predominately by the high-frequency modes ($\hat{\mathcal{T}}_l \ll \hat{\mathcal{T}}_h$). Since

**Table 2. Interfacial Reflectivities and Transmissions**

| interface $ik$ | $R_{ik}^{l}$ | $R_{ki}^{l}$ | $\mathcal{T}_{ik}^{h\ b}$ | $\mathcal{T}_{ki}^{h\ b}$ |
|---|---|---|---|---|
| Si−PS | 0.688 | 0.688 | 0.954 | 0.046 |
| Au−PS | 0.890 | 0.890 | 0.754 | 0.246 |
| PS−air | 0.999 | $\approx 0^{a}$ | 0.949 | |
| Si−air | 1.000 | $\approx 0^{a}$ | 0.997 | |

$^{a}$ See section 4.1. $^{b}$ $\mathcal{T} = 1 - R$.

our model is restricted to the assumption of normal incidence, we have $R_{1p}^{l} = R_{p1}^{l}$, further simplifying the previous equation

$$\bar{Q} \approx \frac{f^3}{1 - f^3} \frac{1}{1 - R_{1p}^{h}} - \frac{1}{2}\left(\frac{u_p}{u_a} - 1\right) \qquad (42)$$

A minor correction concerns the constant $C$ in eqs 37−40. Equation 37 stems from a frequency integration of the specific heat multiplied by the mean free path $\Lambda(\nu)$, $u$ and the temperature gradient.[27] In eq 37, we have replaced $\Lambda(\nu)$ by its average value $\bar{\Lambda}$, which is contained in the constant $C \propto \bar{\Lambda}$. Attenuation measurements in glasses show, however, that $\Lambda \propto \nu^{-x}$, where $x = 1$ for $\nu \lesssim 10$ GHz and $x = 2$ for higher frequencies.[27] A more detailed calculation for $x = 2$ yields a changed value of $f$, while leaving the theoretical model otherwise unchanged. This shifts $\nu_c$ to somewhat smaller frequencies and results in a weaker dependence of $\bar{Q}$ on $\nu_c/\nu_D$. Essentially, low-frequency phonons with large $\Lambda$ contribute more to the thermal conductivity and therefore also to the heat flow compared to the model with $\Lambda = \bar{\Lambda}$.

We now turn to the results of our microscopic calculation (summarized in Table 2) in light of the experiments. The fit of $\bar{Q}$ to the data can be replaced now by a fit of the crossover frequency $\nu_c$ or, correspondingly, by the ratio $f$. Assuming the diffuse mismatch model for $R_{1p}^{h}$ in eq 42, we have $f \approx 0.96$ for the silicon/PS/air/silicon system and $f \approx 0.99$ in the case of the gold substrate. This assumption implies similar values of the crossover frequency $\nu_c$ for the polymer−substrate and polymer air surface. In the case of a higher value of $\nu_c$ for the polymer−substrate interface, eq 32 must be used to evaluate $R_{1p}^{h}$, lowering the $\nu_c$ values by a few percent. The high values of $\nu_c \lesssim \nu_D$ are reasonable. It is noteworthy that despite the high value of $\nu_c$, more than 90% of the heat is transported by high-frequency modes. This is due to the high density of states for $\nu \approx \nu_D$.

**4.4. The Role of the Substrate.** The strong dependence of $\bar{Q}$ on the substrate material is somewhat surprising. Since the only substrate dependent parameter in eq 41 is the substrate−polymer interfacial reflectivity $R_{1p}$, this would imply an unphysically large difference between PS−Au and PS−Si interfacial reflectivities. The large difference in $\bar{Q}$ values lies in a shortcoming of the theory in section 4.2, which we qualitatively address here.

In eqs 37−40, we have modeled the heat flux in terms of the density of states in the polymer layer. By focusing on the polymer layer, the coupling to the substrate enters only via the reflectivity $R_{1p}$. This implies the assumption that the polymer layer equilibrates to establish the Debye density of states, irrespective of the density of states of the adjacent medium. For a polymer film in thermal equilibrium, this assumption is reasonable. The detailed balance of modes is maintained by inelastic phonon scattering processes. For a true non-
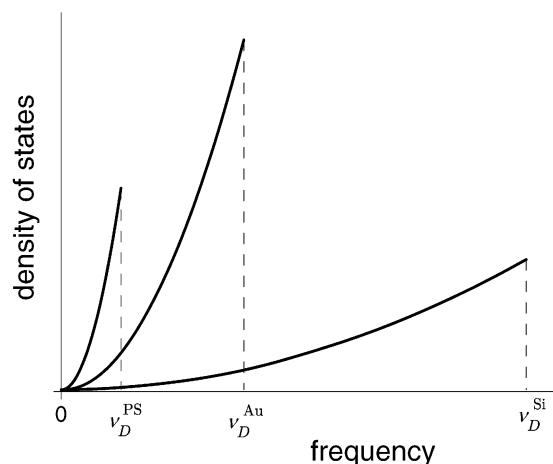


**Figure 9.** Phonon density of states vs frequency for polystyrene, gold, and silicon. In a Debye model, the density of states scales with the square of the frequency.

equilibrium system, however, the detailed balance of states is not necessarily reached. In contrast to high-frequency modes, the scattering probability of 100 GHz phonons is low (due to their long mean free path length), preventing the equilibration of the lower end of the phonon spectrum.

There are two consequences of a distorted phonon spectrum in the lower frequency domain on the film instability reported here. First, since 100 GHz modes do not fully equilibrate, their densities of states depend more directly on the modes coupled in from the substrate. In Figure 9, we have plotted the calculated Debye density of states for PS, Au, and Si. Only a small fraction of the PS modes overlap with the density of states of the gold substrate. The overlap between the density of states of Si and PS is even smaller. This implies that only a small percentage of the thermal modes in the substrate can directly couple into the polymer film. The conduction of heat is dependent on the existence of an efficient frequency down conversion process caused by the inelastic scattering of substrate phonons. While the details of this process are not known,[26] it is evident from Figure 9 that the density of states of PS and Au have a much larger overlap compared to PS and Si, facilitating the direct coupling in of substrate modes. Combined with the long mean free path length of 100 GHz phonons in PS, this leads to a higher PS density of states in this frequency domain for the Au/PS system compared to PS on Si.

A second consequence of the long PS mean free path length in the lower frequency domain could arise from partial phonon resonances in the film. Propagating phonons reflecting from the PS/air interface may be partially back-reflected from the PS/substrate interface, thus reaching the PS/air surface a second time. Similar to the argument above, such partially resonant modes distort (augment) the low-frequency density of states, thereby increasing the phonon induced radiation pressure. Since the reflectivity of the PS/Au interface ($R_{1p}^{l} = 0.89$) is higher compared to the PS/Si interface ($R_{1p}^{l} = 0.69$), a larger phonon resonance effect should occur for the samples with a Au substrate.

Both effects amount to a larger number of low frequency phonon modes in the case of a polymer film on a gold substrate. Since the destabilizing pressure of eq 15 is largely due to these low-frequency modes, the strong dependence of $\bar{Q}$ may have its origin in these two

effects that distort the density of states of the polymer film.

## 5. Conclusions

We have described the morphological transition of a confined liquid polymer film that is caused by an externally imposed temperature gradient. Since the small thickness of our experimental system (a polymer–air double layer) rules out convection, the observed instability at the origin of the morphology change could be linked to the diffusive heat transport through the polymer and air layers. Our experimental results reveal an inverse scaling to the instability wavelength with the heat flux.

By assuming that the system develops toward a steady-state, we note that a polymer configuration that spans the two plates (which act as a heat source and cold sink) maximizes the overall flow of heat through the system. In an equivalent closed system with finite heat capacities of the heat source and cold sink, a polymer morphology that spans the two plates maximizes the equilibration rate of the system.

Our reasoning considers especially the mechanisms of heat transport. Assuming that at least some of the heat is transported across the polymer layer by thermal modes that have a mean-free path comparable to the polymer film thickness, we have developed a phenomenological description that describes the film instability at the origin of the morphology change. In this model, acoustically propagating phonons are reflected off the polymer–air surface, thereby exerting a destabilizing radiation pressure. The predictions of this model reflect the experimentally found $1/J_q$ dependence. The magnitude of the destabilizing effect is, however, determined by a fitting parameter which cannot be predicted in the framework of the phenomenological model.

To make our model more quantitative, a detailed description of the heat transport in both layers and the interfacial coupling at all three interfaces was developed. To this end, the different heat diffusion mechanisms in the polymer and in the air have been taken into account, and the dispersion of thermal modes (or acoustic phonons) was considered. On the basis of an idealized model description we distinguish two different regimes: low frequency modes propagate acoustically and cause a radiation pressure upon reflection off an interface between media of different acoustic impedances. These modes destabilize the film, but contribute only little to the heat transport through the bilayer. Thermal modes close to the Debye limit, on the other hand, are characterized by a very short mean free propagation lengths. These modes scatter constantly and are diffusively transmitted across interfaces. They contribute only little to the force balance at the polymer–air interface, but conduct most of the heat.

This model allows an interesting prediction concerning the stability of liquid films in the setup described here. The long mean free path length of low frequency phonons in polymer films are a consequence of the ambivalent rheological behavior of polymer melts. While liquid on very long times scales (i.e., when imposing a constant shear stress), the molecules are not able to follow rapidly alternating shear fields, due to the entangled nature of the melt. As a consequence, a polymer melt exhibits a glassy rheological behavior at high enough frequencies even at temperatures above their (0 Hz) glass transition temperature. This glassy

rheological behavior is the reason for the relatively long mean free path length of thermal modes in the GHz regime. While this leads to the destabilization of polymer films, as described in this text, films made from low molecular weight liquids should not exhibit this effect since they are lacking the glassy rheological response at high frequencies.

## References and Notes

(1) Cross, M. C.; Hohenberg, P. C. *Rev. Mod. Phys.* **1993**, *65*, 851−1112.
(2) Vrij, A. *Discuss. Faraday Soc.* **1966**, *42*, 23−33.
(3) Brochard-Wyart, F.; Daillant, J. *Can. J. Phys.* **1990**, *68*, 1084−1088.
(4) Reiter, G. *Phys. Rev. Lett.* **1992**, *68*, 75−78.
(5) Jacobs, K.; Herminghaus, S.; Mecke, K. *Langmuir* **1998**, *14*, 965.
(6) Lambooy, P.; Phelan, K. C.; Haugg, O.; Krausch, G. *Phys. Rev. Lett.* **1996**, *76*, 1110−1113.
(7) Reiter, G.; Sharma, A.; Casoli, A.; David, M.-O.; Khanna, R.; Auroy, P. *Langmuir* **1999**, *15*, 2551−2558.
(8) Reiter, G.; Khanna, R.; Sharma, A. *Phys. Rev. Lett.* **2000**, *85*, 1432−1435.
(9) Seemann, R.; Herminghaus, S.; Jacobs, K. *J. Phys.: Condens. Matter* **2001**, 4925.
(10) Bausch, R.; Blossey, R. *Phys. Rev. Lett.* **1994**, *50*, R1759−R1761.
(11) Jacobs, K.; Herminghaus, S.; Mecke, K. R. *Langmuir* **1998**, *14*, 965−969.
(12) Konnur, R.; Kargupta, K.; Sharma, A. *Phys. Rev. Lett.* **2000**, *84*, 931−934.
(13) Wang, C.; Krausch, G.; Geoghegan, M. *Langmuir* **2001**, *17*, 6269.
(14) Herminghaus, S. *Phys. Rev. Lett.* **1999**, *83*, 2359−2361.
(15) Schäffer, E.; Thurn-Albrecht, T.; Russell, T. P.; Steiner, U. *Nature (London)* **2000**, *403*, 874−877.
(16) Schäffer, E.; Thurn-Albrecht, T.; Russell, T. P.; Steiner, U. *Europhys. Lett.* **2001**, *53*, 518−524.
(17) Schäffer, E.; Harkema, S.; Blossey, R.; Steiner, U. *Europhys. Lett.* **2002**, *60*, 255−261.
(18) Sherman, R.; Hirt, D.; Vane, R. *J. Vac. Sci. Technol.* **1994**, *12*, 1876.
(19) Silberzan, P.; Léger, L.; Ausserré, D.; Benattar, J. J. *Langmuir* **1991**, *7*, 1647.
(20) Harkema, S.; Schäffer, E.; Morariu, M. D.; Steiner, U. Submitted to *Adv. Mater.*
(21) Schmittmann, B.; Zia, R. K. P. In *Phase Transitions and Critical Phenomena*; Domb, C., Lebowitz, J. L., Eds.; Academic Press: London, 1995; Vol. 17.
(22) Landau, L. D.; Lifshitz, E. M. *Fluid Mechanics*; Pergamon Press: London, 1959.
(23) Debye, P. *Ann. Phys.* **1912**, *39*, 798−839.
(24) Albanese, C.; Dell'Aversana, P.; Gaeta, F. S. *Phys. Rev. Lett.* **1997**, *79*, 4151−4154.
(25) Stone, M. *arXiv:cond-mat* **2000**, http://arXiv.org/abs/cond-mat/0012316.
(26) Swartz, E. T.; Pohl, R. O. *Rev. Mod. Phys.* **1989**, *61*, 605−668.
(27) Morath, C. J.; Maris, H. J. *Phys. Rev. B* **1996**, *54*, 203−213.
(28) Behrends, R.; Kaatze, U. *J. Phys. Chem. A* **2000**, *104*, 3269−3275.
(29) Sette, F.; Krisch, M. H.; Masciovecchio, C.; Ruocco, G.; Monaco, G. *Science* **1998**, *280*, 1550−1555.
(30) Eisenmenger, W. In *Phonon Scattering at Surfaces and Interfaces V*; Anderson, A. C., Wolfe, J. P., Eds.; Springer: Berlin, 1986; p 112.
(31) Kennard, E. H. *Kinetic theory of gases*; McGraw-Hill Book Co., Inc.: New York, 1938.
(32) Knudsen, M. *Ann. Phys.* **1911**, *34*, 593−656.
(33) Fung, K. H.; Tang, I. N. *Phys. Rev. A* **1988**, *37*, 2557−2561.